Evidence for Hybrid Inorganic–Organic Transitions at the WS₂/Terrylene Interface

Boubacar Tanda Bonkano, Samuel Palato,* Jannis Krumland, Sergey Kovalenko, Philipp Schwendke, Michele Guerrini, Qiuyang Li, Xiaoyang Zhu, Caterina Cocchi, and Julia Stähler*

The realization of the potential of hybrid inorganic organic systems requires an understanding of the coupling between the constituents: its nature and its strength. The observation of hybrid optical transitions in the monolayer WS₂/terrylene hybrid is reported. The first-principle calculations, linear optical, and transient absorption spectroscopy are employed to investigate the optical spectrum of the hybrid, which exhibits a new transition that does not appear in the constituents' spectra. The calculations indicate type II level alignment, with the highest occupied level of terrylene in the gap of WS₂. Exploiting state-resolved transient absorption, the response of the hybrid interface to optical excitation is selectively probed. The dynamics reveal rapid hole transfer from WS₂ to the terrylene layer, with a decay time of 88 ps. This hole transfer induces a bleach of the hybrid transition, which indicates that terrylene contributes to its initial state. Based on this, the hybrid resonance energy, and on our calculations, we assign the hybrid feature to a transition from the highest occupied molecular orbital of terrylene to the conduction band of WS₂ close to the Γ point. The results indicate that the conditions for strong electronic coupling are met in this hybrid system.

1. Introduction

One promising pathway to overcome the limits of silicon-based technology[1–3] is the search for new materials and material combinations with advanced optoelectronic properties going along with simple synthesis and long-term stability. In this context, hybrid systems consisting of inorganic and organic compounds (HIOS) promise to merge the strengths of inorganic and organic semiconductors to produce materials with tailored properties.[2,4] In particular, monolayer transition metal dichalcogenides (TMDCs) provide high charge mobility, a wide, direct bandgap, and are often chemically robust.[5] Recent growth and deposition methods offer unique design opportunities, while their strong susceptibility to their environment enables tuning of the heterostructure properties, whether by encapsulation or coupling.[6–10] The combination of TMDCs with organic semiconductors is, thus, auspicious with regard to useful hybrid properties that go beyond the bare linear combination of the attributes of the separate components.

The performance of hybrid systems leverages interface-specific states and processes such as hybridized electronic levels,[11,12] mixed optical transitions,[13–15] charge separation and migration,[16,17] and interlayer excitons.[18,19] For example, trapping the charges at the interface into interlayer excitons can be detrimental for light-harvesting applications. Conversely, the same interlayer excitons enrich the emission spectrum at longer wavelengths and could thus be exploited for sensing applications. The occurrence and strength of such phenomena depend crucially on the energy level alignment, the resulting wave function overlaps as well as on the electronic coupling strength of the constituents. These determine not only

B. Tanda Bonkano, S. Palato, S. Kovalenko, P. Schwendke, J. Stähler
Institut für Chemie and IRIS Adlershof
Humboldt-Universität zu Berlin
12489 Berlin, Germany
E-mail: samuel.palato@hu-berlin.de; julia.staehler@hu-berlin.de

B. Tanda Bonkano, S. Palato, S. Kovalenko, P. Schwendke, J. Stähler
Abt. Physikalische Chemie
Fritz-Haber-Institut der Max-Planck-Gesellschaft
14195 Berlin, Germany

J. Krumland, M. Guerrini, C. Cocchi
Physics Department and IRIS Adlershof
Humboldt-Universität zu Berlin
12489 Berlin, Germany

M. Guerrini, C. Cocchi
Institute of Physics and Center for Nanoscale Dynamics
Carl von Ossietzky Universität Oldenburg
26129 Oldenburg, Germany

Q. Li, X. Zhu
Department of Chemistry
Columbia University
New York, NY 10027, USA

whether energy levels hybridize, but also if (bright) optical transitions result and how far charge and energy transfer processes lead to the formation, decay, or bleach of excited hybrid states and transitions. It is the complexity of HIOS that generates a fragile balance between several counter-acting processes that may or may not lead to hybrid signatures in a given system. This is why—despite a plethora of experimental and theoretical studies on combinations of different TMDCs,[8,20,21] TMDC/organic interfaces,[22] and combinations of these with nanoparticles[23–25]—a complete understanding of this complex and sensitive interplay has still not been achieved. To tackle this issue, it is useful to combine complementary experimental techniques with theory and identify systems that allow for the disentanglement of elementary processes.

The detection and characterization of hybrid features are in many cases challenging, in particular on the basis of steady-state spectroscopy. The bare observation of new peaks in an absorption spectrum is not necessarily an unambiguous proof of the hybrid character of the transition, as differences in growth conditions and changes to the dielectric environment can simply cause optical resonances to (dis-)appear. One way to obtain additional information on the character of a new transition is the use of ultrafast spectroscopy,[26–29] which probes the changes of the sample properties under nonequilibrium conditions after photoexcitation and allows the educated choice of excitation energy that selectively excites different transitions and/or regions in the sample.

Here, we report on the observation of hybrid excitations and dynamics at the WS_2/terrylene interface using linear and transient absorption spectroscopy in combination with ab initio calculations. A new transition at 2.6 eV is observed in the hybrid system using steady-state spectroscopy. Based on first-principles calculations of the energy levels, which indicate type II alignment, and on the measurement of the response of the hybrid to interface-specific excitation, we can assign this new spectral feature to a hybrid transition between the terrylene HOMO and the WS_2 conduction band (CB) near the Γ point of the Brillouin zone where it exhibits enough sulfur character to allow for orbital overlap with the organic. Furthermore, we observe that selective excitation of the WS_2 A exciton is followed by ultrafast hole transfer to the terrylene HOMO within 200 fs. The recombination of electrons and holes occurs on the significantly longer timescale of 88 ps due to the large excess energy that needs to be dissipated in this process. It can be concluded that the WS_2/terrylene system exhibits a broad selection of hybrid features and, thus, is a useful model system to study the interaction of organic and TMDC materials.

2. Results

Figure 1a shows a scheme of the sample under study. The sample consists of a monolayer WS_2 flake on fused silica obtained by the gold tape exfoliation method,[6] onto which a terrylene film with a nominal thickness of 10 nm (gray area) was deposited by evaporation using a Knudsen cell (see Methods section). A representative thickness measurement by atomic force microscopy (AFM) is shown in Figure 1b. The morphology of the terrylene film shows small grains with a diameter of $\approx$100 nm. Both, WS_2 and terrylene, absorb in the visible range.
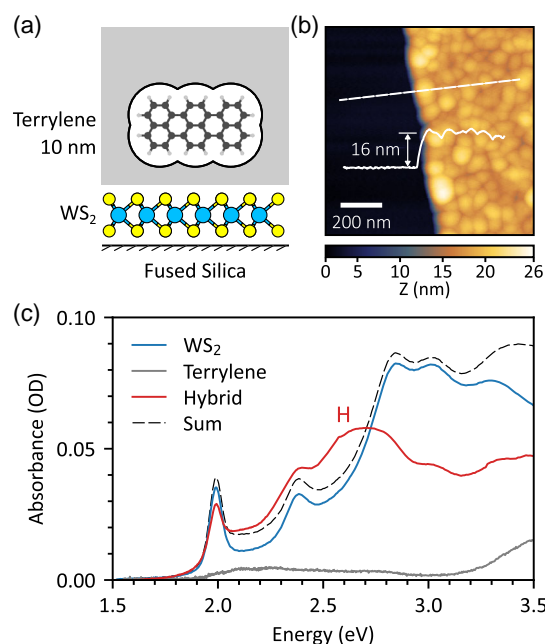

Figure 1. Hybrid WS_2/terrylene system. a) Scheme of the sample. b) AFM image of the terrylene layer on WS_2. c) Absorption spectrum of the hybrid system and individual constituents. In the absence of interactions, the former spectrum should be the sum of the two contributions. A new feature located at 2.6 eV is visible in the hybrid system.

The WS_2/terrylene hybrid system is, therefore, expected to exhibit rich dynamics arising from coupling and charge transfer.

Figure 1c shows the absorption spectrum of the hybrid alongside the spectra of the individual components. We first review the spectroscopic response of the individual components. The optical spectroscopy of monolayer WS_2 has been studied extensively (see, e.g.,[9,30–33]), which is why we only briefly summarize the main features here. Figure 1c shows the absorption spectrum of monolayer WS_2 on fused silica obtained by gold-tape exfoliation, in blue.[6] It is characterized by a series of absorption peaks associated with bright excitons, called A (1.99 eV), B (2.38 eV), and C (2.83 eV). The A and B excitons originate from vertical transitions at the K point of the Brillouin zone. The energy difference between the two excitons is mainly due to spin-orbit coupling separating the valence band (VB) into two sub-bands at the K point (see **Figure 2**). The C band has been assigned to direct transitions located along Γ–K axis of the Brillouin zone and enhanced by band nesting.[34,35] Excitonic properties play a crucial role in the electronic structure and optical properties of monolayer WS_2.

The spectroscopic properties of terrylene are intermediate between those of its smaller and larger siblings: perylene and quaterrylene. Figure 1c shows the spectrum of the terrylene film deposited on a fused silica substrate in gray. The absorption spectrum of isolated terrylene molecules in *p*-xylene solution exhibits the standard response of polycyclic aromatic hydrocarbons, with a strong absorption at 2.22 eV and a characteristic Franck–Condon lineshape due to coupling to ring distortion modes (see Figure S1, Supporting Information).[36,37] Aggregation of terrylene enables strong intermolecular interactions which
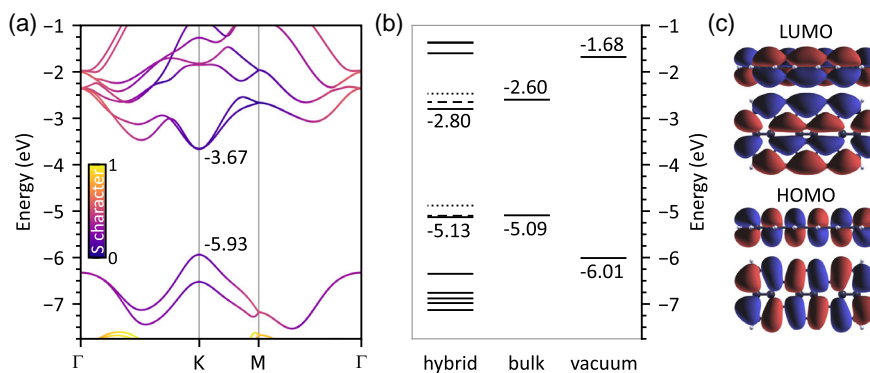
Figure 2. Calculation of the electronic structure of WS$_2$ and terrylene in the hybrid. All energies are referenced to vacuum. a) Band diagram of monolayer WS$_2$ calculated using DFT. The bands are colored according to their contribution from the S orbitals. Renormalization due to screening in the hetero-structure is included. b) Energy of the molecular orbitals (MOs) of terrylene in vacuum (right), of the terrylene film (bulk) and of the hybrid (hybrid). The energy levels of the frontier orbitals at the interface are shown for three orientations of the molecule: face-on (solid), edge-on (dashed), and end-on (dotted). MOs from LUMO + 3 to HOMO-5 in the face-on geometry are also shown. LUMO + 2 and LUMO + 3 are closely spaced and appear as a single line. c) Frontier orbitals of terrylene. The isovalue is set to $0.02a_0^{-3/2}$.

significantly modifies the optical and electronic properties. The intermolecular interactions are strongly dependent on film crystallinity and packing geometry.[38] The spectrum of the film shown in Figure 1c is broadened compared to the solution, consistent with its disordered and polycrystalline morphology. The suppression of the 0-0 vibrational line and the overall reduction in absorbance is consistent with H aggregation in our sample[39] and its partially ordered nature.

Having presented the spectra of the individual components, we now discuss the spectrum of the hybrid. In the absence of interactions, the spectrum of the hybrid should be similar to the sum of the individual components, which is shown by the dashed spectrum in Figure 1c. Comparing the spectrum of the hybrid to this independent sum reveals similarities and differences. In the visible range, features associated with the A and B excitons of WS$_2$ are clearly visible. Although there are changes in amplitude, the shape and position of the A and B transitions are not modified. For energies larger than 2.7 eV, the absorption of the hybrid is reduced with respect to the absorption of WS$_2$. This effect persists over the entire bandwidth available to us (up to 6 eV, see Figure S2, Supporting Information) and will not be discussed further here. Despite this change in magnitude, features associated with the C exciton peaks are visible in the hybrid. Deeper into the UV, the absorption features of the hybrid system align with the absorption peaks of the terrylene film (see Figure S2, Supporting Information). At energies larger than 2.7 eV, the spectrum of the hybrid therefore resembles the spectrum of non-interacting components, albeit with a reduced amplitude. The excitonic features of WS$_2$ are, therefore, still present in the hybrid and generally undisturbed.

In addition to these similarities, a new feature is visible in the spectrum of the hybrid system. It manifests as an increase in absorbance centered at 2.6 eV. It has no correspondence to any absorption feature of the isolated components, nor their sum. This absorption band is, therefore, a new excitation allowed exclusively in the hybrid system. We designate this new transition as the H band as it occurs in the hybrid sample. Its spectral position and width are difficult to extract as it is located in a

region of the WS$_2$ spectrum with many overlapping contributions. Detailed modeling of the WS$_2$ spectrum requires the inclusion of weak signals from the higher B excitons (2S, 2P, etc.). Multiple bands also contribute to the region of the C exciton.[9,40] Extracting spectral parameters for the H band is therefore challenging. A fit to the spectrum of the H band results in an estimated position of 2.6 eV and a FWHM of 294 meV (see Figure S3, Supporting Information). Our model likely overestimates the width and amplitude of the band, as it does not include the higher B exciton states. Nevertheless, the width is comparable to literature values for the width of the B and C excitons in WS$_2$.[9,40]

It is not possible to assign this transition from the absorption spectrum only; it may have interfacial character, but could also result from structural modifications of the terrylene film. Further information is required to an interfacial transition and to gain insights into the underlying processes. In the following, we review the standard optical coupling mechanisms, perform calculations of the electronic structure of the hybrid, and measure the nonequilibrium response of the film to optical excitation at the interface to gain insights into the nature of the H band and understand the electronic structure of the hybrid system. The final assignment of the H band to a hybrid transition will be rationalized in the Discussion section.

Two standard coupling mechanisms can give rise to the new transition when two materials interact.[39,41] The first is dipole–dipole coupling, also known as Kasha coupling. When two oscillating dipoles are brought in close proximity, they interact through space, being in each other's electric field. The coupling strength J_{ab} depends on the geometrical arrangement of the two dipoles $\boldsymbol{\mu_a}$ and $\boldsymbol{\mu_b}$ according to

$$J_{ab} = \frac{\boldsymbol{\mu_a} \cdot \boldsymbol{\mu_b} - 3(\boldsymbol{\mu_a} \cdot \hat{r})(\boldsymbol{\mu_b} \cdot \hat{r})}{4\pi\varepsilon r_{ab}^3} \tag{1}$$

where r_{ab} is the distance between the two dipoles, $\hat{r}$ is the corresponding unit vector, ε is the dielectric constant of the medium, and $\boldsymbol{\mu_{a,b}}$ are the transition dipole moments of the

spectroscopic transitions. When the coupling is large, dipole–dipole coupling can result in the mixing of the two electronic transitions, and therefore to delocalized excitons. This causes a symmetrical shift of the transitions and redistribution of the transition moments.[41] Critically, the strength of dipole–dipole coupling is proportional to $|\mu_a||\mu_b|$. It therefore vanishes for dark transitions.

Hybrid spectroscopic transitions can also occur by direct transitions between the energy levels of the two constituents. This phenomenon can give rise to new optical transitions which are not a simple combination of the optical transitions of the components. In the absence of scattering and after subtraction of reflection losses, the absorbance is proportional to the absorption coefficient α, given by

$$\alpha(\nu) \propto \sum_{i,f} \nu_{fi} |\mu_{fi}|^2 G(\nu - \nu_{fi}) \tag{2}$$

where $\nu = E/h$ is the optical frequency, $\nu_{fi} = (E_f - E_i)/h$ is the energy difference between the final (f) and initial states (i), expressed as a frequency, μ_{fi} is the transition dipole moment for the $i \rightarrow f$ transition, and $G(\nu)$ is a lineshape function with unit area. μ_{fi} is given by

$$\mu_{fi} = q_e \int \varphi_f^\dagger(r) \hat{r} \varphi_i(r) d^3r \tag{3}$$

where q_e is the elementary charge, $\varphi(r)$ are the wavefunctions, and $\hat{r}$ is the position operator. Equation (3) demonstrates the known fact that optical transitions require spatial overlap of the two wavefunctions, and, hence, of the corresponding electron densities. In a hybrid system, this can either occur due to overlap of the wavefunctions of the two components, or if at least one of the orbitals is hybridized and extends across both constituents, the second case implying the first.[11] In addition to spatial overlap, the optical transition must obey the standard selection rules: it must be momentum-direct as well as spin- and symmetry-allowed. Symmetry breaking at the interface makes the latter condition more readily met than in bulk media.[42]

To understand the spectrum of the hybrid system and the dynamics, it is necessary to know the electronic structure of the constituents and their relative alignment. Figure 2 shows the results of ab initio and electrostatic calculations of the individual components and heterostructure. Figure 2a shows the band diagram of WS_2 calculated from first principles. The color of the bands indicates their sulfur character. Bands with low sulfur contribution (blue) are located on the d orbitals of the W atoms, at the center of the monolayer. They, therefore, do not overlap with the π orbitals of the organic layer and are thus less susceptible to coupling in the heterostructure, whether for orbital hybridization or for a spectroscopic transition. Due to their atomic thickness, monolayer transition metal dichalcogenides are highly sensitive to dielectric screening by their environment.[7,9,30] We include the screening of both the substrate and the terrylene layer (see below and Methods section). This contribution symmetrically shifts the band extrema at the K-point, reducing the bandgap by 0.32 eV. This effect is already included in the the band diagram in Figure 2a.

Figure 2b shows the energy of the molecular orbitals (MOs) of terrylene. First, we compute the energies for an isolated molecule in vacuum (right) using density functional theory (DFT, see Methods section). For a more accurate estimation of the energy levels in the bulk terrylene film, we include screening by the surrounding terrylene environment. Using real-time time-dependent DFT of a terrylene molecule in a polarizable medium, we estimate the dielectric constant of bulk terrylene as $\varepsilon = 3.2$ (see Methods section). This reduces the calculated gap between the highest occupied molecular orbital (HOMO) and the lowest unoccupied molecular orbital (LUMO) of an embedded terrylene molecule to 1.84 eV. This calculation neglects aggregation effects that are important in the electronic and excitonic properties of organic films, such as dipole–dipole and charge transfer coupling.[39] However, it should provide a reasonable estimate of the gas-to-crystal shift and provide a good starting point from which to understand the aggregate.

We further calculate the impact of electrostatic screening on the energy of the terrylene orbitals at the hybrid interface using LayerPCM.[43] The geometry used in the calculations is the same as for WS_2 (see Methods section for details). As the interface is anisotropic, the energies of the MOs depend on the orientation of the terrylene molecule relative to the interface. Figure 2b shows the results for the face-on (solid lines), edge-on (dashed lines), and end-on (dotted lines) orientations. Screening at the interface further reduces the HOMO–LUMO gap and shifts the energies of the frontier orbitals differently with respect to bulk terrylene, but the variations of the gap size are small. In the face-on geometry, both the HOMO and the LUMO lie at lower energies than in the bulk film. Conversely, in the end-on geometry, both states lie at higher energies than in the bulk. The edge-on geometry shows intermediate results. This variation in band alignment provides opposite driving forces for charge migration to and from the interface, depending on local geometry.

States beyond the frontier orbitals and band edges can also participate in hybridization at the interface. Figure 2b also shows the energies for states ranging from HOMO-5 to LUMO + 3. The occupied (virtual) states were shifted keeping their energy difference to the HOMO (LUMO) constant. All terrylene orbitals in this energy region have π character. The isosurface of the LUMO and HOMO are shown in Figure 2c. The different MOs of terrylene occupy the same spatial region both above and below the molecule's plane, albeit with distinct nodal patterns.

Figure 2a,b represents the best estimate available to us for the energy level alignment of the WS_2 monolayer and terrylene film at the interface. These calculations were shown to have a similar accuracy to more expensive methods, while further including the geometry of the heterostructure.[44] However, these calculations do not include microscopic effects such as interface dipoles that cause charge transfer across the interface due to Fermi energy alignment. In the case of the similar perylene molecule on WS_2, calculations reveal an interfacial dipole pulling electrons toward WS_2.[11] In the absence of polar chemical bonds of chemisorbed molecules and without permanent dipole moments in the adsorbed species, such interfacial dipoles typically lead to energy shifts of few 100 meV or less.[45] As our calculations indicate that the WS_2/terrylene interface exhibits type-II alignment with a HOMO-VB energy difference of ≈ 0.80 eV and a

CB-LUMO separation of ≈0.87 eV, such minor shifts due to interfacial dipoles should not affect the general type-II alignment. Thus, our calculations indicate the WS$_2$/terrylene hybrid system should favor charge separation after optical excitation, with electrons accumulating in the TMDC monolayer and holes in terrylene, potentially migrating into the film. Note that the LUMO of terrylene is located within the bandwidth of the lowest CB of WS$_2$, favoring chemical hybridization. Similarly, the HOMO-1 to HOMO-5 states are located within the highest VB, and are likely candidates for the formation of hybrid states.[11]

To assess whether charge separation occurs and to gain further insights into the hybrid state, the relaxation of the system to photoexcitation is measured via transient absorption (TA) spectroscopy. The sample is first photoexcited using an ultrashort laser pulse resonant with specific transitions in the sample, in our case resonant with the WS$_2$ A exciton. A broadband probe laser pulse then monitors the change in the absorbance of the sample following photoexcitation.[46] The experiment is repeated at various pump-probe delays to measure the relaxation dynamics in the sample. The experiment thus measures changes in the absorbance of the sample ΔA as a function of both probe energy and pump-probe time delay, for specific excitation conditions. In TA spectroscopy, a negative signal corresponds to a reduction in the absorbance (bleach), which can be due to a depletion of the ground state (ground-state bleach, GSB) or due to stimulated emission. A positive signal indicates an increase in the absorbance, termed excited-state absorption (ESA). A signal can also arise when the position or shape of a spectroscopic resonance is perturbed in the excited state, even if its total transition dipole moment is not reduced. For example, a shift of the resonance toward lower energy (red-shift) yields a positive value of ΔA on the low-energy side and a negative value of ΔA on the high-energy side. In this case, the TA spectrum has a shape similar to the derivative of the absorption spectrum. The transient spectra measured at different time delays give valuable information regarding shifts of the energy levels and population dynamics.

In TA, careful selection of the excitation conditions enables the control of the initial excited state. This ability to specify the initial population has been exploited extensively to study processes ranging from chemical reactions to carrier relaxation in confined semiconductors.[47–51] In all experiments reported here, we used an excitation resonant with the A exciton. The A exciton is the lowest electronic excitation, therefore, this state has access to less relaxation channels. Furthermore, as the terrylene film is transparent at the wavelength of the A exciton, this excitation condition selectively excites the WS$_2$ monolayer film and enables us to selectively probe the response of the interfacial region. Our TA experiments are, therefore, interface-specific. **Figure 3**a shows the TA spectra obtained from the WS$_2$ monolayer on fused silica and the hybrid sample at selected time delays. Comparing the response of the isolated WS$_2$ monolayer to the hybrid system provides insights into the dynamics in the hybrid.

We start by analyzing the spectrum of WS$_2$. The spectrum, shown in Figure 3a, bottom, reveals derivative lineshapes at the positions of the A, B and C excitons, which correspond to a red-shift of the resonances. At early time delays, the A transition shows a net bleach contribution. These results are
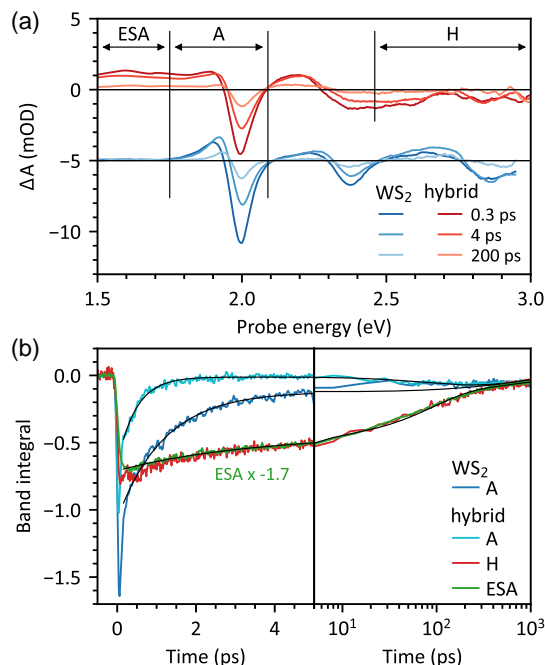
Figure 3. Dynamics of WS$_2$ and hybrid following excitation resonant with the A exciton. a) Transient spectra at selected time delays for WS$_2$ (bottom) and the hybrid system (top). Spectra of WS$_2$ offset for clarity. b) Dynamics of the band integrals. The positions and boundaries of the band integrals are indicated in panel (a).

in agreement with previous results obtained in similar fluence range.[31,32,52–55] (See Figure S4, Supporting Information for the entire traces.) As the time delay is increased, the amplitude decreases, but the overall spectral shape remains the same.

Figure 3a also shows the results obtained for the hybrid system using similar excitation conditions, i.e., only the A exciton is populated while the spectral response of the hybrid is monitored. Some similarities exist with the signal from WS$_2$. The A exciton shows a bleach signal and signatures of a small red-shift. A derivative-like feature is also apparent around the position of the B exciton, although the feature is less defined. This can be attributed mainly to the overlap with a broader bleach signal at higher energies. A faint derivative feature can also be observed at 2.8 eV, the position of the C exciton. In addition to these similarities, a broad ESA continuum arises below the energy of the A exciton. Furthermore, a bleach signal at 2.6 eV overlaps with the signals of the B and C exciton. This net bleach signal indicates a bleach of the H transition. Thus, exciting the A state of WS$_2$ leads to both a bleach of the H transition and an absorption continuum below the A exciton.

To gain further insights into the origin of these signals, we analyze the excited state kinetics. To do so, we compute band integrals. The band integral I is defined as

$$I(t) = \frac{1}{\ln(\nu_2/\nu_1)} \int_{\nu_1}^{\nu_2} \frac{\Delta A(t)}{\nu} \, d\nu \quad (4)$$

where t is the pump-probe time delay, ν_1 and ν_2 are the boundaries of the band, ΔA is the change of absorbance, and ν is the

frequency.[56,57] Careful selection of the boundaries enables the selection of specific contributions. When the band encompasses an entire absorption feature, the band integral is proportional to the change in the transition dipole moment of the ensemble (see Equation (2)). Therefore, selecting a band that covers the entire width of a shifting peak removes the contribution from the peak shift to the dynamics and isolates the net change in absorption coefficient.[58] We make use of this property to remove the contribution from the peak shifts of the A, B, and C excitons to the dynamics.

The selected band integrals and their boundaries are shown on Figure 3a. The bands were selected to isolate specific contributions arising from the A exciton, ESA continuum, and hybrid state. For the A band, the boundaries encompass the entirety of A exciton transition, including the shifted transition at early delays. This band integral, therefore, isolates the reduction in the absorption of the A exciton irrespective of peak shifts. The same boundaries are used for the band integral of the A excitons of WS_2 and the hybrid. The ESA band is located on the low-energy side of the A band and extends to the lower edge of our detection bandwidth. The H band integral is located above the signal from the B exciton, and contains the shifting C exciton. Selecting these boundaries therefore removes the contribution of the peak shift of the C excitons from the dynamics. This band integral thus reveals the dynamics of the bleach of the H transition. In all cases, it was verified that the resulting kinetic transients are not sensitive to minor changes of the boundaries. For completeness, it should be noted that, in the case of the ESA continuum, the decay is homogeneous over the selected range. In the case of the H band integral, identical results can be obtained by selecting thin bands between the B and C excitons or above the C exciton, albeit with a worse signal-to-noise ratio.

The resulting kinetics are shown on Figure 3b. To facilitate comparison, the ESA band was multiplied by -1.7. The signals from the A bands of WS_2 and the hybrid sample (light and dark blue) show qualitatively similar kinetics. The net bleach of the A exciton decays within the first few ps after excitation. These kinetic profiles correspond to the recovery of the oscillator strength of the A exciton, and are therefore related to decay of the population of the bright A exciton as well as scattering of secondary charge carriers away from contributing bands. The faster rate in the hybrid system is consistent with additional relaxation pathways for excitons and charge carriers in the hybrid system compared to the WS_2 monolayer.

By contrast, the ESA continuum (green) and the H transition (red) exhibit much slower dynamics. The signals appear almost instantaneously. A fast build-up component is visible in the first 200 fs of the ESA band. Most of the decay occurs on the timescale of tens of ps. Critically, their decay profile is nearly identical. There is a small discrepancy before 2 ps, which we assign to the imperfect cancellation of the C exciton peak shift in the H band integral. The identical behavior of the two decay profiles indicates the ESA and bleach of the H transition arise from the same excited population.

The timescales of the dynamics are quantified by curve fitting. The resulting fits are shown as black lines on Figure 3b. In all cases, a tail fit is performed, excluding the first 150 fs. The early part of the signal is contaminated by extra contributions from coherent processes due to the overlap of the pump and the probe

Table 1. Time constants for the global decay models. Numbers in parentheses indicate the uncertainty on the last two digits.

Sample	τ_A [ps]	τ_1 [ps]	τ_2 [ps]	τ_{long} [ns]
WS_2	1.20(15)	–	–	0.74(44)
Hybrid	0.473(60)	3.07(40)	88(10)	1.14(26)

pulses.[41,46,59] The decay of the A exciton in WS_2 is fitted with a biexponential decay with time constant τ_A for the fast decay component and τ_{long} for the slow decay component.

The three kinetic transients from the hybrid state are fitted globally with a total of four exponential functions (see methods section), albeit not all of them contributing to all kinetic traces equally as discussed in detail in the Experimental section. The time constants are τ_A for early delays, τ_1, τ_2 for intermediate delays and τ_{long} for decays on very long timescales. The results are collected in **Table 1**. The constant τ_A is associated with the early time delays of the A band integral in the hybrid sample, and is given the same interpretation for WS_2 and the hybrid. The time constant τ_1 is involved mainly in peak shift dynamics, which we do not analyze here.[32] The time constant τ_{long} is weak and poorly sampled here. The time constant $\tau_2 = 88$ ps occurs mainly in the ESA and H band integrals, which share kinetics over the entire measured time range, and will be discussed further below.

3. Discussion

The observations can be summed up as follows. First-principles calculations accounting for screening in the heterostructure indicate type-II level alignment, with the HOMO of terrylene located in the bandgap of WS_2. The LUMO overlaps with the CB of WS_2, while the first few occupied states below the HOMO overlap with the VB. These states are therefore candidates for hybridization with the WS_2 states. Hybridization is further favored for bands which have a significant contribution of S orbitals.[11] The presence of the HOMO in the gap opens up the possibility of novel transitions between the HOMO and the CB of WS_2.

The absorption spectrum of the hybrid sample exhibits signatures of the A, B, and C excitons of WS_2. The energies of the A and B excitons are not significantly perturbed. The absorption spectrum of the hybrid exhibits a new absorption feature called H, located at 2.6 eV, between the B and C excitons. Selective excitation of the interface is achieved by tuning the excitation wavelength to resonance with the A exciton of WS_2. The H band responds to this excitation with a magnitude similar to the excitons from WS_2. Therefore, the H band must be localized at the interface. As it is only observed in the hybrid, it must arise from the interaction of terrylene and WS_2.

Two mechanisms can mediate the interaction: dipole–dipole coupling and transitions involving both components of the hybrid. Dipole–dipole type coupling can be ruled out for two reasons: the coupling strength is proportional to the transition dipole moment, which is very weak for terrylene in this spectral region (see Equation (1)). Furthermore, dipole–dipole coupling has specific phenomenological signatures: a symmetric shift

of the participating transitions and conservation of the total peak areas. Our sample does not conform to either of these traits. The new feature, therefore, arises from a hybrid transition. The observation of this hybrid transition implies orbital overlap or delocalization as a necessary condition. The response of the H band to excitation of the WS_2 monolayer confirms its interfacial nature, and the coupling mechanism implies strong electronic coupling in the hybrid.

Selective excitation of the A exciton in the WS_2 monolayer gives rise to different dynamics in the TA data of the hybrid sample. While the relaxation of the WS_2 features remains qualitatively similar, the hybrid sample exhibits two extra optical signals in the hybrid system: an ESA continuum below the A exciton resonance energy and a bleach of the H transition. Both new features show an ultrafast build-up within the first 200 fs and decay with identical kinetics. The decay kinetics is dominated by a time constant of 88 ps.

We explain these observations using the scheme shown in **Figure 4**. In this figure, the energy of the A exciton is displayed on the band diagram to facilitate comparison, even though excitons are not formally part of the same basis as electrons and holes. We placed the A exciton energy as it would be probed in a photoemission experiment, by aligning all the states with respect to the vacuum level. An equivalent alignment can be obtained by aligning the ground state in the exciton basis (so-called exciton vacuum) with the top of the valence band.

From the optical spectrum, we observe that the energies of the A and B exciton are not perturbed, which implies the band extrema at the K point do not couple directly to terrylene states. This can be explained both by energy level alignment and by the low sulfur character of the contributing bands, localizing them inside the WS_2 monolayer around the W atoms.

Our assignment of the H transition is based on the results of the TA experiment. As emphasized above, the excitation pulse was selected to exclusively generate a population of A excitons, at the interface. This process is indicated by the blue arrow. The H band responds to these excitation conditions within only 200 fs and thus the corresponding transition must be located at interface. The electron and hole states forming the A exciton
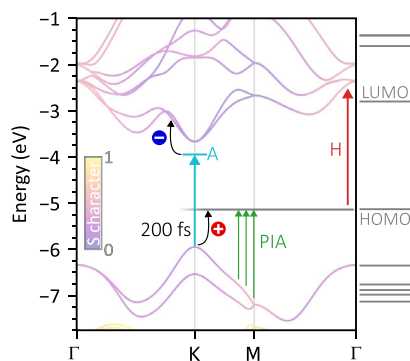
Figure 4. Processes and spectroscopic observables in the hybrid system. Note that energy levels are aligned with respect to the vacuum level, which allows to indicate the energy of the A exciton (two particles) in the single-particle band structure of WS_2. This is the energy at which the electron of the A exciton would be probed in a two-photon photoemission experiment.

are located at the K point. The relaxation kinetics of the A exciton bleach differ from those of the H transition bleach. Therefore, these two transitions do not share a population. This rules out the possibility that the H transition occurs from the top of the VB, or into the minimum of the CB. Furthermore, as the excitation is localized inside the WS_2 monolayer (d orbitals of W at the K point), the response of the H transition indicates that the corresponding states are located at the interface, and that the H transition is not a property of the bulk film, such as a different crystal structure in the hybrid.

Type II level alignment permits the transfer of the hole of the A exciton to the HOMO of terrylene. This is a new relaxation channel available in the hybrid for the relaxation of holes at the top of the VB. The transfer of part of the A exciton hole population across the interface to the HOMO of the terrylene molecules is indicated by the black arrow. The occurrence of this process is consistent with the abrupt bleach of the H transition and appearance of the ESA continuum, which occurs within the first 200 fs after excitation, as discussed below. This process releases enough energy (≈ 0.8 eV, c.f. results section) to unbind the exciton and promote the corresponding electron into the free-particle CB of WS_2. Once the holes have transferred to the HOMO, new transitions from the deeper VBs of WS_2 to the HOMO (electron vacancy) become possible, which is consistent with the flat shape and energy distribution of the ESA continuum. Due to the comparably large contribution of sulfur orbitals to the VBs in this part of the electronic band structure, the M point is a likely candidate (green arrows in Figure 4). The energy of the VB at the M point overlaps with the energy of the HOMO-2 to HOMO-5 states, which favors mixing of these states. Mixing is expected to enhance the oscillator strength of this transition. We also note that the terrylene radical cation has spectroscopic transitions in this spectral region.[37] The ESA continuum at low energies is therefore consistent with hole transfer to the terrylene film.

Simultaneously, the hole population in the HOMO of the terrylene molecules bleaches the H transition, indicating that the initial state of the H resonance is the HOMO. The hole transfer thus explains both observations, the H transition bleach and the ESA continuum - as well as their coinciding dynamics. The energy of the H resonance is larger than both the HOMO–LUMO gap of WS_2 and the $S_0 \rightarrow S_1$ transition in terrylene. The $S_0 \rightarrow S_2$ transition is located at 3.6 eV and is symmetry forbidden. Therefore, we assign the H transition at 2.6 eV to a transition from the HOMO of terrylene to the CB of WS_2. This assignment is supported by the energy of the transition, the spectral features of the TA spectra, and the different dynamics of the A exciton and H band bleaches. We further suggest that this transition is located at or close to the Γ point. According to our first-principles calculations, the energy of 2.6 eV closely matches the energy difference between the HOMO and the CB at Γ. Furthermore, the high contribution of S orbitals to the CB at Γ enhances orbital overlap between the two components, favoring hybrid transitions. This transition is bleached when holes have transferred from the WS_2 to the terrylene HOMO and recovers once these holes are filled with electrons after 88 s. Thus, we assign the H band to a hybrid transition between the HOMO of terrylene and the CB of WS_2, with the Γ point as the most likely candidate.

At a first glance, the quite substantial difference of hole and electron transfer times from WS_2 to the terrylene film might appear counter-intuitive. However, the side conditions of these two processes differ significantly: in the case of the hole transfer, ≈800 meV have to dissipated, while, at the same time, the electron of the A exciton needs to be lifted by several 100 meV to a dispersive single particle state in the WS_2 CB. In other words, the energy dissipation channel of the hole transfer process is already built-in, due to the excitonic character of the initial state. In the case of the electron transfer, the situation is vastly different: the electron and hole are on different sides of the interface. Recombination requires again a quite substantial energy release of ≈1 eV or more, however, there are no directly related quasi-particles that could absorb this energy as in the previous case. It is not enough energy for across band gap excitations, leaving only Auger-type scattering processes with carriers in the WS_2 and energy release via light emission in the near-infrared, similar to previous studies on inorganic/organic hybrid systems.[13,15,60,61] Keeping in mind that the electrons are localized in the CB minimum at the K point of the Brillouin zone, Figure 4 indicates that the WS_2 band structure offers only very few final states for Auger-type scattering processes that could account for the energy loss of ≳1 eV. In any case, they require large momentum changes. Based on this, it seems highly likely, that the slow recombination time across the interface is associated with a bright hybrid transition, possibly preceded by hybrid exciton formation.

All of our key observations: the H transition observed in the absorption spectrum, the ESA continuum observed in TA, the ultrafast hole transfer, and the electron-hole recombination across the interface indicate strong coupling in this TMDC-organic hybrid system. Our results suggest that hybrids can further be used to engineer optoelectronic properties by charge separation and lifetime enhancement of photogenerated carriers.

4. Conclusion

We investigated a hybrid inorganic–organic system consisting of a terrylene film on monolayer WS_2. First-principle calculations indicate type-II alignment with the HOMO of the terrylene molecules located in the WS_2 gap. Linear and time-resolved optical spectroscopy reveal the presence of new transitions as well as ultrafast charge transfer processes in the hybrid upon photoexcitation resonant with the WS_2 A exciton. The transitions are assigned to hybrid transitions where the orbitals of both components participate. In particular, a new transition H at 2.6 eV is assigned to a dipole-allowed hybrid exciton formed of the HOMO of terrylene and the CB of WS_2 in the vicinity of the Γ point. In transient absorption, this transition is bleached after hole transfer from the TMDC to the terrylene HOMO, which occurs in 200 fs. Concurrently, a photo-induced absorption continuum at low energies builds up and is assigned to a transition from the VB of WS_2 to holes in the HOMOs of terrylene film. This is followed by recombination via electron transfer from the WS_2 CB at the Γ-point to the terrylene in 88 ps, potentially preceded by interlayer exciton formation. The occurrence of these transitions indicates spatial overlap of the orbitals of the inorganic and organic components of the hybrid. The terrylene/WS_2 hybrid system, thus, not only meets the conditions for strong electronic coupling. Due to the numerous, clearly distinguishable hybrid features, the terrylene/WS_2 is an interesting model system to systematically modify and study hybrid phenomena.

5. Experimental Section

Deposition of the Terrylene Film: The synthesis of terrylene was carried out following a route published previously.[36] Final purification was carried out by multiple subsequent steps of crystallization from 1,2,4-trichlorobenzene and sublimation. The terrylene film was deposited with the help of a Knudsen cell under ultrahigh vacuum conditions. The procedure was identical for terrylene on a fused silica substrate and for the hybrid sample (terrylene/WS_2/fused silica). The deposition process was monitored using a precalibrated quartz microbalance.[62] Evaporation was carried out at a crucible temperature of 244 °C and a chamber pressure of 2×10^{-19} mbar. The onset temperature for evaporation of terrylene was 204 °C. The substrate was kept at 300 K. The evaporation was carried out at an average rate of 0.5 nm min^{-1}. The resulting film covered the substrate uniformly. The thicknesses of the terrylene films were measured by AFM in tapping mode (amplitude: 35 nm, Arrow NCPt tip). A thin scratch was made on the sample using tweezers. The edges were measured in multiple locations yielding results ranging from 7 nm at the edge of the substrate to 16 nm toward the center.

Ab Initio Calculations: Electronic properties are determined with density functional theory. The band structure of free-standing WS_2 is calculated with the plane-wave-based Quantum ESPRESSO[63] and Wannier90 codes,[64] adopting the PBE0 hybrid functional.[65] The band structure is centered around the mid-gap energy predicted by PBE.[66] This approach is based on the finding that PBE0 gives reasonable estimates for bandgaps of transition metal dichalcogenides, but poor ones the mid-gap position, while the opposite is true for PBE.[44] PBE-based norm-conserving and fully relativistic SG15 pseudopotentials are employed,[67,68] k- and q-grids of 12×12 and 6×6 are used, respectively, the latter sampling the Brillouin zone for the evaluation of the exact-exchange integrals. Plane-wave kinetic energy cutoffs are set to 40, 160, and 120 Ry for wave functions, density, and Fock exchange, respectively. Hexagonal lattice constants are taken to be $a = 3.19$Å and $c = 20$Å, thus introducing a large vacuum layer decoupling the replica in the out-of-plane direction.

The bandgap renormalization due to screening is calculated by solving Poisson's equation for a point charge situated in a dielectric slab of thickness 5.35 Å representing WS_2, sandwiched between semi-infinite dielectrics corresponding to the substrate and the aggregate.[44] These media are separated from the WS_2 slab by 0.95 Å of vacuum each. The dielectric constant of the fused silica substrate is taken to be $\varepsilon_s = 3.9$, while those of WS_2 ($\varepsilon_\perp = 11.33$, $\varepsilon_\parallel = 15.21$) and the aggregate ($\varepsilon_a = 3.2$) are calculated from first principles, as described in the next paragraph. The bandgap renormalization is estimated as the difference between the electrostatic polarization potential at the position of the added point charge with and without encapsulating media.[69] It arises in equal parts from a decrease of the conduction band energies and an increase of valence band ones.

The dielectric constants $\varepsilon_\perp$ and $\varepsilon_\parallel$ of WS_2 are computed with the random-phase approximation atop a PBE electronic structure, using the Yambo code[70] with 200 conduction bands and a plane-wave cutoff of 6 Ry. The dielectric constant ε_a of the aggregate is estimated with time-dependent density functional theory on the adiabatic PBE level, as implemented in the real-time, real-space code Octopus.[71] The bulk aggregate is modeled as a terrylene molecule inside a cavity carved into a bulk dielectric. It is excited by an impulsive electric field $E(t) = \kappa \delta(t)$, where κ is the "kick strength", and evolved in time; local field effects are included and furnish the dipole with a dependence on the dielectric constant of the surrounding polarizable medium, $d = d(\varepsilon_a)$. The microscopic molecular polarizability is inferred from the induced dipole moment and translated into a macroscopic dielectric function with a Clausius–Mossotti-like equation

$$\varepsilon_a = \frac{4\pi d(\varepsilon_a)}{\kappa V} + 1 \qquad (5)$$

where V is the volume of the cavity, which is constructed by interlocking spheres centered at all atoms with the respective van der Waals radius scaled by a factor of 1.2. The dielectric constant ε_a set for the surrounding medium is adjusted until the resulting dipole moment d satisfies Equation (5).

The frontier levels of a terrylene unit in the aggregate are determined with the LayerPCM extension of Octopus.[43] The ionization potential, equal to the negative of HOMO energy, is the total energy difference between the neutral molecule and the (electronically relaxed) single cation; the electron affinity, i.e., the LUMO energy, is the total energy difference between the neutral molecule and the single anion. As both ions are open shell, corresponding total energy calculations are performed without spin restriction. Screening effects due to the surrounding media are implicitly included through the reaction potential in the Kohn–Sham Hamiltonian. Shifting occupied and virtual orbitals from PBE until the Kohn–Sham HOMO and LUMO energies match the values from total energy differences, we obtain estimates also for the energies of nonfrontier orbitals. In all Octopus calculations, the simulation box is constructed as the union of atom-spheres with radii 5 Å and subsequently sampled with a grid with spacing 0.2 Å in each direction. Consistent with the Quantum ESPRESSO calculations, PBE is used for exchange and correlation in conjunction with SG15 pseudopotentials.

Transient Absorption: The transient absorption spectrometer has been described in details previously.[46,72] The instrument is driven by a Ti: Sapphire chirped pulse amplifier (CPA) with a central wavelength of 800 nm. The excitation pulse is generated by frequency doubling the signal output of a tunable optical parametric amplifier. The probe beam is generated by focusing part of the 800 nm beam into a CaF2 plate. The instrument employs chopping and single-shot referencing to achieve high signal-to-noise ratio.

For the results presented here, the excitation pulses had energies of 50 nJ pulse^{-1} for WS_2 and 36 nJ pulse^{-1} for the WS_2/terrylene hybrid. The radius of the excitation beam at the sample is estimated to 250 µm. The radius of the probe beam is less than half this size. The excitation fluences are 59 µJ cm^{-2} for WS_2 and 36 µJ cm^{-2} for the hybrid. Using the absorbance values from the spectra on Figure 1c yields nominal excitation densities on the order of 1.6×10^{13} cm^{-2} for WS_2 and 7.7×10^{12} cm^{-2} for the hybrid, neglecting optical saturation effects. The pump-probe time delay was scanned in steps of 0.02, 4 and 8 ps. For each sample, eight scans were averaged to increase the signal-to-noise ratio. The polarization of the pump and probe beams were parallel.

The kinetics of the band integrals of the hybrid are fitted globally using a sum of exponential decays. The model is expressed as follows

$$I_i(t) = \sum_j a_{ij} \exp[-t/\tau_j] \qquad (6)$$

where $I_i(t)$ is the band integral, i indexes the band integrals, j indexes the components, a_{ij} is the amplitude matrix and τ_j are the time constants. The fit includes a total of four bands integrals: the ESA, A and H band integrals, as well as the band integral located between the A and H integrals. This latter band is included in the global fit to extract the kinetics but not analyzed, as its profile is sensitive to the exact location of the boundaries. The use of four kinetic curves for four components is also standard in global fitting procedures.[73] Left to its own devices, the fitting algorithms have difficulty separating the four exponential components. However, the early time component τ_A is clearly independent of the others. Therefore, we constrain the matrix a_{ij} to better separate this contribution. The amplitudes for τ_A is constrained to 0 for all band integrals except I_A. The amplitudes for decay τ_1 is constrained to 0 for the A band integral. These simple constraints enable the algorithms to correctly fit τ_A, yielding results similar to an independent fit of I_A. The use of a global fit for the other three components enable the algorithm to converge robustly for all of them. The curve fit is performed by least-squares minimization using

the Nelder–Mead simplex algorithm. The fit is refined by Markov-chain Monte Carlo sampling of the posterior distribution of parameters, yielding statistically equivalent results.

Supporting Information

Supporting Information is available from the Wiley Online Library or from the author.

Conflict of Interest

The authors declare no conflict of interest.

Data Availability Statement

The data that support the findings of this study are available from the corresponding author upon reasonable request.

[1] L. C. Andreani, A. Bozzola, P. Kowalczewski, M. Liscidini, L. Redorici, *Adv. Phys. X* **2019**, *4*, 1548305.

[2] M. Wright, A. Uddin, *Sol. Energy Mater. Sol. Cells* **2012**, *107*, 87.

[3] A. Polman, M. Knight, E. C. Garnett, B. Ehrler, W. C. Sinke, *Science* **2016**, *352*, aad4424.

[4] R. Schlesinger, F. Bianchi, S. Blumstengel, C. Christodoulou, R. Ovsyannikov, B. Kobin, K. Moudgil, S. Barlow, S. Hecht, S. Marder, F. Henneberger, N. Koch, *Nat. Commun.* **2015**, *6*, 6754.

[5] Q. H. Wang, K. Kalantar-Zadeh, A. Kis, J. N. Coleman, M. S. Strano, *Nat. Nanotechnol.* **2012**, *7*, 699.

[6] F. Liu, W. Wu, Y. Bai, S. H. Chae, Q. Li, J. Wang, J. Hone, X.-Y. Zhu, *Science* **2020**, *367*, 903.

[7] Y. Xu, S. Liu, D. A. Rhodes, K. Watanabe, T. Taniguchi, J. Hone, V. Elser, K. F. Mak, J. Shan, *Nature* **2020**, *587*, 214.

[8] J. Gu, L. Ma, S. Liu, K. Watanabe, T. Taniguchi, J. C. Hone, J. Shan, K. F. Mak, *Nat. Phys.* **2022**, *18*, 395.

[9] N. Ansari, F. Ghorbani, *J. Opt. Soc. Am. B* **2018**, *35*, 1179.

[10] E. Najafidehaghani, Z. Gan, A. George, T. Lehnert, G. Q. Ngo, C. Neumann, T. Bucher, I. Staude, D. Kaiser, T. Vogl, U. Hübner, U. Kaiser, F. Eilenberger, A. Turchanin, *Adv. Funct. Mater.* **2021**, *31*, 2101086.

[11] J. Krumland, C. Cocchi, *Electron. Struct.* **2021**, *3*, 044003.

[12] M. Jacobs, J. Krumland, C. Cocchi, *ACS Appl. Nano Mater.* **2022**, *5*, 5187.

[13] U. Hörmann, S. Zeiske, S. Park, T. Schultz, S. Kickhöfel, U. Scherf, S. Blumstengel, N. Koch, D. Neher, *Appl. Phys. Lett.* **2019**, *114*, 183301.

[14] M. Eyer, J. Frisch, S. Sadofev, N. Koch, E. J. W. List-Kratochvil, S. Blumstengel, *J. Phys. Chem. C* **2017**, *121*, 21955.

[15] F. Piersimoni, R. Schlesinger, J. Benduhn, D. Spoltore, S. Reiter, I. Lange, N. Koch, K. Vandewal, D. Neher, *J. Phys. Chem. Lett.* **2015**, *6*, 500.

[16] C. Strothkämper, A. Bartelt, P. Sippel, T. Hannappel, R. Schütz, R. Eichberger, *J. Phys. Chem. C* **2013**, *117*, 17901.

[17] J. Sobus, G. Burdzinski, J. Karolczak, J. Idígoras, J. A. Anta, M. Ziólek, *Langmuir* **2014**, *30*, 2505.

[18] E. Yalon, C. J. McClellan, K. K. Smithe, M. Muñoz Rojo, R. L. Xu, S. V. Suryavanshi, A. J. Gabourie, C. M. Neumann, F. Xiong, A. B. Farimani, E. Pop, *Nano Lett.* **2017**, *17*, 3429.

[19] C. R. Lien-Medrano, F. P. Bonafé, C. Y. Yam, C. A. Palma, C. G. Sánchez, T. Frauenheim, *Nano Lett.* **2022**, *22*, 911.

[20] M. Plankl, P. E. Faria Junior, F. Mooshammer, T. Siday, M. Zizlsperger, F. Sandner, F. Schiegl, S. Maier, M. A. Huber, M. Gmitra, J. Fabian, J. L. Boland, T. L. Cocker, R. Huber, *Nat. Photonics* **2021**, *15*, 594.

[21] P. Nagler, G. Plechinger, M. V. Ballottin, A. Mitioglu, S. Meier, N. Paradiso, C. Strunk, A. Chernikov, P. C. Christianen, C. Schüller, T. Korn, *2D Mater.* **2017**, *4*, 2.

[22] S. B. Homan, V. K. Sangwan, I. Balla, H. Bergeron, E. A. Weiss, M. C. Hersam, *Nano Lett.* **2017**, *17*, 164.

[23] M. W. Brett, C. K. Gordon, J. Hardy, N. J. L. K. Davis, *ACS Phys. Chem. Au* **2022**, *2*, 364.

[24] I. A. M. Al-Ani, K. As'ham, O. Klochan, H. T. Hattori, L. Huang, A. E. Miroshnichenko, *J. Opt.* **2022**, *24*, 053001.

[25] M. Guizzardi, M. Ghini, A. Villa, L. Rebecchi, Q. Li, G. Mancini, F. Marangi, A. M. Ross, X. Zhu, I. Kriegel, F. Scotognella, *J. Phys. Chem. Lett.* **2022**, *13*, 9903.

[26] K. Stallberg, A. Namgalies, S. Chatterjee, U. Höfer, *J. Phys. Chem. C* **2022**, *126*, 12728.

[27] Z. Xu, Y. Zhou, C. Y. Yam, L. Groß, A. De Sio, T. Frauenheim, C. Lienau, G. Chen, *Sci. Adv.* **2021**, *7*, eabf7672.

[28] L. Gierster, O. Turkina, J.-C. Deinert, S. Vempati, E. Bowen Dodoo, Y. Garmshausen, S. Hecht, C. Draxl, J. Stähler, How Hybrid Excitons Suppress Charge Separation: Ultrafast, but Delayed, **2023**.

[29] X. Zhu, N. R. Monahan, Z. Gong, H. Zhu, K. W. Williams, C. A. Nelson, *J. Am. Chem. Soc.* **2015**, *137*, 8313.

[30] G. Wang, A. Chernikov, M. M. Glazov, T. F. Heinz, X. Marie, T. Amand, B. Urbaszek, *Rev. Mod. Phys.* **2018**, *90*, 021001.

[31] S. Calati, Q. Li, X. Zhu, J. Stähler, *Phys. Rev. B* **2023**, *107*, 115404.

[32] S. Calati, Q. Li, X. Zhu, J. Stähler, *Phys. Chem. Chem. Phys.* **2021**, *23*, 22640.

[33] A. Chernikov, C. Ruppert, H. M. Hill, A. F. Rigosi, T. F. Heinz, *Nat. Photonics* **2015**, *9*, 466.

[34] D. Kozawa, R. Kumar, A. Carvalho, K. Kumar Amara, W. Zhao, S. Wang, M. Toh, R. M. Ribeiro, A. H. Castro Neto, K. Matsuda, G. Eda, *Nat. Commun.* **2014**, *5*, 4543.

[35] T. Goswami, H. Bhatt, K. J. Babu, G. Kaur, N. Ghorai, H. N. Ghosh, *J. Phys. Chem. Lett.* **2021**, *12*, 6526.

[36] Y. Avlasevich, C. Kohl, K. Müllen, *J. Mater. Chem.* **2006**, *16*, 1053.

[37] T. M. Halasinski, J. L. Weisman, R. Ruiterkamp, T. J. Lee, F. Salama, M. Head-Gordon, *J. Phys. Chem. A* **2003**, *107*, 3660.

[38] S. W. Eaton, S. A. Miller, E. A. Margulies, L. E. Shoer, R. D. Schaller, M. R. Wasielewski, *J. Phys. Chem. A* **2015**, *119*, 4151.

[39] N. J. Hestand, F. C. Spano, *Chem. Rev.* **2018**, *118*, 7069.

[40] Y. Li, A. Chernikov, X. Zhang, A. Rigosi, H. M. Hill, A. M. Van Der Zande, D. A. Chenet, E. M. Shih, J. Hone, T. F. Heinz, *Phys. Rev. B: Condens. Matter Mater. Phys.* **2014**, *90*, 1.

[41] P. Hamm, M. Zanni, *Concepts And Methods Of 2D Infrared Spectroscopy*, vol. *9781107000*, Cambridge University Press, Cambridge, **2011**.

[42] A. M. Kelley, *J. Chem. Phys.* **2020**, *152*, 12.

[43] J. Krumland, G. Gil, S. Corni, C. Cocchi, *J. Chem. Phys.* **2021**, *154*, 224114.

[44] J. Krumland, C. Cocchi, Electronic Structure of Low-Dimensional Inorganic/Organic Interfaces: Hybrid Density Functional Theory, G_0W_0, and Electrostatic Models, **2023**.

[45] J. Stähler, P. Rinke, *Chem. Phys.* **2017**, *485–486*, 149.

[46] S. A. Kovalenko, A. L. Dobryakov, J. Ruthmann, N. P. Ernsting, *Phys. Rev. A* **1999**, *59*, 2369.

[47] C. B. Moore, I. W. M. Smith, *J. Phys. Chem.* **1996**, *100*, 12848.

[48] S. Palato, H. Seiler, H. Baker, C. Sonnichsen, P. Brosseau, P. Kambhampati, *J. Chem. Phys.* **2020**, *152*, 10.

[49] C. D. Sonnichsen, J. Kipp, X. Tang, P. Kambhampati, *ACS Photonics* **2018**, *6* 382.

[50] G. Grimaldi, J. J. Geuchies, W. van der Stam, I. du Fossé, B. Brynjarsson, N. Kirkwood, S. Kinge, L. D. Siebbeles, A. J. Houtepen, *Nano Lett.* **2019**, *19*, 3002.

[51] S. L. Sewall, R. R. Cooney, E. A. Dias, P. Tyagi, P. Kambhampati, *Phys. Rev. B* **2011**, *84*, 235304.

[52] S. Dal Conte, C. Trovatello, C. Gadermaier, G. Cerullo, *Trends Chem.* **2020**, *2*, 28.

[53] L. Wang, W. Wang, Q. Wang, X. Chi, Z. Kang, Q. Zhou, L. Pan, H. Zhang, Y. Wang, *RSC Adv.* **2019**, *9*, 37195.

[54] P. D. Cunningham, K. M. McCreary, B. T. Jonker, *J. Phys. Chem. Lett.* **2016**, *7*, 5242.

[55] L. T. Lloyd, R. E. Wood, F. Mujid, S. Sohoni, K. L. Ji, P.-C. Ting, J. S. Higgins, J. Park, G. S. Engel, *ACS Nano* **2021**, *15*, 10253.

[56] M. T. Quick, M. Quick, I. N. Ioffe, C. Richter, R. Mahrwald, S. Druzhinin, S. A. Kovalenko, *J. Phys. Chem. B* **2020**, *124*, 1049.

[57] J. Moreno, A. L. Dobryakov, I. N. Ioffe, A. A. Granovsky, S. Hecht, S. A. Kovalenko, *J. Chem. Phys.* **2015**, *143*, 024311.

[58] S. A. Kovalenko, R. Schanz, H. Hennig, N. P. Ernsting, *J. Chem. Phys.* **2001**, *115*, 3256.

[59] P. Brosseau, H. Seiler, S. Palato, C. Sonnichsen, H. Baker, E. Socie, D. Strandell, P. Kambhampati, *J. Chem. Phys.* **2023**, *158*, 084201.

[60] U. Hörmann, S. Zeiske, F. Piersimoni, L. Hoffmann, R. Schlesinger, N. Koch, T. Riedl, D. Andrienko, D. Neher, *Phys. Rev. B* **2018**, *98*, 155312.

[61] M. Raoufi, S. Chandrabose, R. Wang, B. Sun, N. Zorn Morales, S. Shoaee, S. Blumstengel, N. Koch, E. List-Kratochvil, D. Neher, *J. Phys. Chem. C* **2023**, *127*, 5866.

[62] S. Vempati, J.-C. Deinert, L. Gierster, L. Bogner, C. Richter, N. Mutz, S. Blumstengel, A. Zykov, S. Kowarik, Y. Garmshausen, J. Hildebrandt, S. Hecht, J. Stähler, *J. Phys. Condens. Matter* **2019**, *31*, 094001.

[63] P. Giannozzi, O. Baseggio, P. Bonfà, D. Brunato, R. Car, I. Carnimeo, C. Cavazzoni, S. de Gironcoli, P. Delugas, F. Ferrari Ruffino, A. Ferretti, N. Marzari, I. Timrov, A. Urru, S. Baroni, *J. Chem. Phys.* **2020**, *152*, 154105.

[64] G. Pizzi, V. Vitale, R. Arita, S. Blügel, F. Freimuth, G. Géranton, M. Gibertini, D. Gresch, C. Johnson, T. Koretsune, J. Ibañez-Azpiroz, H. Lee, J.-M. Lihm, D. A. Marrazzo, Y. Mokrousov, J. I. Mustafa, Y. Nohara, Y. Nomura, L. Paulatto, S. Poncé, T. Ponweiser, J. Qiao, F. Thöle, S. S. Tsirkin, M. Wierzbowska, N. Marzari, D. I. Souza, A. A. Mostofi, et al., *J. Phys. Condens. Matter* **2020**, *32*, 165902.

[65] C. Adamo, V. Barone, *J. Chem. Phys.* **1999**, *110*, 6158.

[66] J. P. Perdew, K. Burke, M. Ernzerhof, *Phys. Rev. Lett.* **1996**, *77*, 3865.

[67] M. Schlipf, F. Gygi, *Comput. Phys. Commun.* **2015**, *196*, 36.

[68] P. Scherpelz, M. Govoni, I. Hamada, G. Galli, *J. Chem. Theory Comput.* **2016**, *12*, 3523.

[69] Y. Cho, T. C. Berkelbach, *Phys. Rev. B* **2018**, *97*, 041409.

[70] D. Sangalli, A. Ferretti, H. Miranda, C. Attaccalite, I. Marri, E. Cannuccia, P. Melo, M. Marsili, F. Paleari, A. Marrazzo, G. Prandini, P. Bonfà, M. O. Atambo, F. Affinito, M. Palummo, A. Molina-Sánchez, C. Hogan, M. Grüning, D. Varsano, A. Marini, *J. Phys. Condens. Matter* **2019**, *31*, 325902.

[71] N. Tancogne-Dejean, M. J. T. Oliveira, X. Andrade, H. Appel, C. H. Borca, G. Le Breton, F. Buchholz, A. Castro, S. Corni, A. A. Correa, U. De Giovannini, A. Delgado, F. G. Eich, J. Flick, G. Gil, A. Gomez, N. Helbig, H. Hübener, R. Jestädt, J. Jornet-Somoza, A. H. Larsen, I. V. Lebedeva, M. Lüders, M. A. L. Marques, S. T. Ohlmann, S. Pipolo, M. Rampp, C. A. Rozzi, D. A. Strubbe, et al., *J. Chem. Phys.* **2020**, *152*, 124119.

[72] A. L. Dobryakov, S. A. Kovalenko, A. Weigel, J. L. Pérez-Lustres, J. Lange, A. Müller, N. P. Ernsting, *Rev. Sci. Instrum.* **2010**, *81*, 113106.

[73] J. E. Loefroth, *J. Phys. Chem.* **1986**, *90*, 1160.